







Ceramic Additive Manufactured Monolithic X-Shaped TM Dual-Mode Filter

DANIEL MIEK ¹ (Student Member, IEEE), MICHAEL HÖFT ¹ (Senior Member, IEEE),
JOSE ANTONIO LORENTE², ANDRE BERGER², DOMINIK BROUCZEK³, MARTIN SCHWENTENWEIN ³,
ANA BRANDAO ⁴, PETRONILO MARTÍN-IGLESIAS ⁴ (Member, IEEE),
AND VITTORIO TORNIELLI DI CRESTVOLANT ⁴ (Member, IEEE)

(Regular Paper)

¹Kiel University, 24143 Kiel, Germany

²Tesat Spacecom, 71522 Backnang, Germany

³Lithoz GmbH, 1060 Vienna, Austria

⁴ESA, 2201, AZ Noordwijk, The Netherlands

CORRESPONDING AUTHOR: Daniel Miek (dami@tf.uni-kiel.de).

This work was supported by the European Space Agency (ESA) under Grant 4000123748/18/NL/HK.

ABSTRACT This paper presents a monolithic 3D-printed ceramic X-shaped dual-mode microwave filter. The filter is manufactured utilizing a lithography-based ceramic manufacturing (LCM) process, allowing the realization of the resonator as well as the housing in one single piece. Therefore, contact as well as alignment problems, usually arising between a ceramic in *TM* mode operation and a metallic enclosure, can conveniently be avoided. A fourth order dual-mode filter with a designed center frequency of 6 GHz and a bandwidth of 279 MHz is realized in alumina material. Practical design rules to be considered in the filter layout process as well as limitations imposed by the LCM approach are discussed. The outer surface of the ceramic cavity is subsequently metallized using a silver spray-coating. Advantageously, the metallization is only a few micrometers thick, wherefore the weight of the component can be reduced. The measurement results are compared to the simulation and reveal good agreement. A temperature stability measurement shows a center frequency downward shift of 0.22%.

INDEX TERMS 3D-printed ceramic filter, additive manufacturing, alumina 3D printing, dielectric TM dual-mode filter, monolithic ceramic filter.

I. INTRODUCTION

Dielectric or ceramic filters were first described in 1939 by Richtmyer [1]. However, first applications in the area of microwave resonators and filters based on ceramics arise several decades later due to manufacturing issues associated with the temperature stability of the ceramic materials [2]. Nowadays, dielectric filters are key components in e.g. communication systems. In comparison to waveguide filters, they can have a drastically reduced volume while maintaining a high Q-factor [3]. Depending on the arrangement of the dielectric resonator in the cavity, different modes of operation must be distinguished.

The $TE_{01\delta}$ mode is often used as fundamental mode and offers a very high Q-factor which mainly depends on

the properties of the ceramic material. The electric field is concentrated in the dielectric resonator, which has no contact to the surrounding metallic cavity and is mounted on a low permittivity material [4]. The ceramics used for this application are almost traditionally pressed in suitable molds and sintered afterwards. This is a meaningful approach for simple geometries and mass production. Restrictions arise, if dual- or multi-mode resonators with specialized shape should be manufactured from ceramic materials. Examples can be found in e.g. [5], where a dual-mode resonator based on two degenerated $TE_{01\delta}$ modes is realized. There, at least one ceramic is cut and subsequently connected with the other one. For this approach, alignment issues as well as potential sources of loss must be considered to prevent a decreased Q-factor. Based

on a similar concept, spherical triple TE mode resonators are proposed in [6]. The manufacturing of these resonators with the classical approach might be extremely sophisticated and cost intensive. An alternative approach for the realization of these ceramics is additive manufacturing (AM), commonly known as 3D printing. Nearly arbitrary formed shapes might be realized by AM. Advantageously, the fabrication costs only depend on the required material as well as on the production time, but are independent from the geometrical shape.

Depending on the material to be processed, different AM technologies are available. Microwave filters manufactured out of plastic material are a common approach for the light-weight realization of complex waveguide resonator structures, e.g. [7], [8]. These filters are often realized with the stereolithography approach, where an UV laser is used to cure a resin at positions defined by the CAD file of the component to be manufactured. A similar but more complex approach can be used for the manufacturing of ceramic resonators and filters.

Based on the layer-by-layer ceramic stereolithography approach, different types of microwave filters were already released, including filters based on a grid shape [9], [10] and cubic as well as octagonal shaped resonators [11], [12]. In comparison to the classical approach, no alignment problems arise if the base plate, support structures as well as the resonator are manufactured in one piece. In [11] the shielding cavity of a single resonator was manufactured from alumina material as well and subsequently metallized. This allows, for example, the optimization of the resonator geometry or support structures with respect to the Q-factor or the spurious free region into unconventional shapes, which might not be realizable with classical manufacturing techniques.

Resonators operating in the TM mode are another option for the implementation of microwave filters [13], [14], which might benefit from the AM approach. They offer a comparably large spurious free region but require a proper contact between the ceramic resonator and the (usually metallic) surrounding housing. This material transition may contribute a majority of the insertion loss if it is not properly designed, especially in environments with strongly varying ambient temperatures. A common approach is to clamp the ceramic rods into the housing, which additionally might lead to cracks if the pressure is too high. The problem becomes more severe when dual- or multi-mode resonators and filters are fabricated using a similar approach, as e.g. in [15]–[17]. The simultaneous realization of a good electrical contact between each ceramic and the surrounding housing is the main challenge. One solution might be the manufacturing of monolithic resonators, where the housing is made from the same material. This approach was already accomplished by conventional techniques [18], [19], but might be restrictive for more sophisticated geometries.

The realization of nearly arbitrarily shaped resonators/filters can only be fulfilled by employing additive manufacturing techniques rather than by conventional shaping methods. Especially TM mode filters might benefit from this

approach as alignment issues between a ceramic rod and the housing as well as thermal contact problems can be avoided. Based on AM, second order TM mode filters were already realized in [20]–[22], where a metallic paint is applied to the exterior of the cavity housing. Similar studies are accomplished in [23].

Considering these advancements, this paper proposes the design, realization and measurement results of a fourth order monolithic dual-mode filter in TM mode operation. To the best of the authors knowledge, this is the first time a monolithic TM mode ceramic filter with complex shape and a filter order larger than two is presented. The fabricated filter reveals a center frequency of roughly 6 GHz and a bandwidth of 202 MHz. The filter is based on two X-shaped dual-mode resonators, similar as proposed in [15], [24] or even [25]. However, contact as well as alignment problems are conveniently avoided by using the LCM additive manufacturing approach.

This paper is organized as follows: Section II gives an overview over the ceramic additive manufacturing process applied for the realization of the filter. Subsequently, Section III describes the filter design process as well as design rules imposed by the manufacturing process. The measurement results are compared to the simulation in Section IV, followed by a temperature stability measurement. Finally, Section V summarizes and concludes this paper.

II. CERAMIC ADDITIVE MANUFACTURING

The shaping of ceramic materials is a central issue and a wide variety of processes were proposed until now. The commonly known approaches include casting, injection moulding and pressing of ceramic materials. Most of these “classical” processes are either extremely expensive especially for small batch numbers, have long lead times or are not suitable for the production of complex ceramic geometries.

Additive manufacturing reveals a meaningful alternative for the realization of geometries with complex shape. Within AM, the process of producing a component begins with a digital 3D model. This model is sliced into individual layers with a pre-defined layer-height using dedicated software. This choice must be in accordance with the specifications of the applied additive manufacturing process. In the manufacturing machine (the 3D printer), the real component is created layer-by-layer from this information.

Different ceramic AM approaches are discussed in the literature. Within the area of microwave components, a stereolithography based approach was recently used for the manufacturing of resonators and filters [9]–[12], [26]–[29].

In the first step, a ceramic powder with desired electrical and/or mechanical properties is mixed with a binder, realizing a slurry. The binder is required in the photopolymerization process and connects adjacent ceramic particles if exposed to UV light. In the stereolithography approach an UV laser is used to cure the ceramic slurry located on the top of the building platform. The diameter of the laser spot, the layer height as well as the precision of the optical system mainly define the manufacturing accuracy. After finishing one layer,

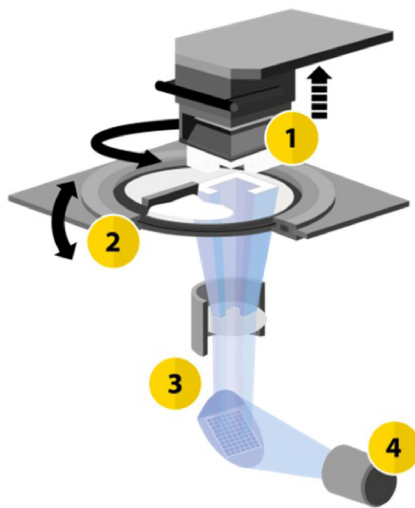


FIGURE 1. Schematic drawing of the LCM printing process: (1) building platform, (2) rotating vat, (3) optical system, and (4) LED [21].

the building platform is lowered by one layer height, new material is released and the process repeats. Advantageously, the manufactured component is recessed in the ceramic slurry, which reduces the requirement for complex support structures during the printing process. Otherwise, a printing job requires a large amount of ceramic slurry, which might be rehashed after finishing the component. Furthermore, the area to be cured is rasterized by the laser, which might lead to a long printing duration for large components.

An alternative is offered by the digital light processing (DLP) approach [21], [30]. The basic working principle is similar to stereolithography and visualized in Fig. 1. A LED-array (4) with wavelength of 460 nm is used as a light source. The light is projected using a digital micromirror device (DMD) as well as an optical system (3) into the direction of the rotating vat (2), where the building platform (1) is located. Depending on the appearance of the layer to be printed, each mirror in the DMD is either turned “on” or “off”. Ceramic material is only cured in the corresponding pixel, if the mirror is turned on. After printing a layer, the building platform moves upwards, followed by a vat rotation, and a wiper blade is used to reapply the slurry. Finally, the building platform is lowered again and a new layer is exposed to light and thus connected to the previous one.

Concerning tolerances arising in the ceramic AM process, one has to distinguish between lateral tolerances and those arising in building direction. The 3D design to be printed is uploaded as stl format and sliced into 2D images using the machine software. The number of images generated depends on the selected slice thickness (which corresponds to the thickness of a printed layer). If the height of the component is not integer divisible by the selected slice thickness, it is either rounded up (if the difference is larger or equal to half of the selected layer thickness) or rounded down (if the difference is smaller than half of the layer thickness). For a selected layer thickness of e.g. 20 μm , the maximum error is $\pm 10 \mu\text{m}$ for

the height of the printed component. Depending on the design and utilized material, layer thicknesses between 10 μm and 100 μm can be realized.

During the slicing process, the intersection curves between a plane (at a certain height) and all intersecting triangles are calculated. The sum of all intersecting lines gives the contour of the part at a given height. These contour lines are overlaid with the pixel grid of the build platform. If more than half of a given pixel is covered by the contour line, that pixel is on. If this is not the case, the pixel is off. For the CeraFab System S65 with a pixel size of 40 x 40 μm^2 , the maximum deviation in XY direction is thus $\pm 20 \mu\text{m}$.

Scattered light generated during the exposure of a layer (the extent depends on the exposure energy and the material) can lead to an enlargement of the component in XY direction (known as over-polymerization), which, however, can be compensated by geometry correction parameters and/or through optimized exposure energy.

After 3D printing, the component is called a green part. The structural support is formed by the binder, a cross-linked photopolymer, in which the ceramic particles are embedded as filler. The green part does not yet have any ceramic properties. The green parts must undergo a thermal post-treatment to finally obtain a dense ceramic after sintering. In order to achieve the desired dimensions, the designs are printed with appropriate scaling factors, which are determined at the beginning of each material development based on a test series. For the alumina material used in this work, these shrinkage compensation factors are 1.233 in XY and 1.273 in Z direction. After sintering, the shrinkage of the component reduces the systematic deviation which can occur during the printing process as described above. Through a suitable design and an optimized parameter setup, components can finally be produced with a very high dimensional accuracy, with dimensional deviations in a range smaller 10 μm .

In comparison to the former mentioned stereolithography principle, the DLP approach is able to print a whole layer instantaneously without rastering the surface, leading to a reduced printing time. Additionally, the required amount of slurry is reduced to a minimum due to the bottom-up principle. Otherwise, the building platform is removed from the vat after printing every single layer, leading to pull-off forces at the printed component. It is therefore required to design components which are in agreement with this printing process. It must additionally be mentioned that different building envelopes are available, ranging from 64 x 40 x 320 mm up to 192 x 120 x 320 mm. As for all printers the same DMD is used, the lateral resolution decreases from 25 μm (small building envelope) to 75 μm (large envelope).

After printing, a cleaning step is applied, whereby any supporting structures or excess material adhering to the component is removed. The component (green part) is then heated in a special furnace so that the binder thermally decomposes (debinding). In order to avoid cracks and spallings during the debinding, it is required that the material thickness remains below a certain limit, which mainly depends on the

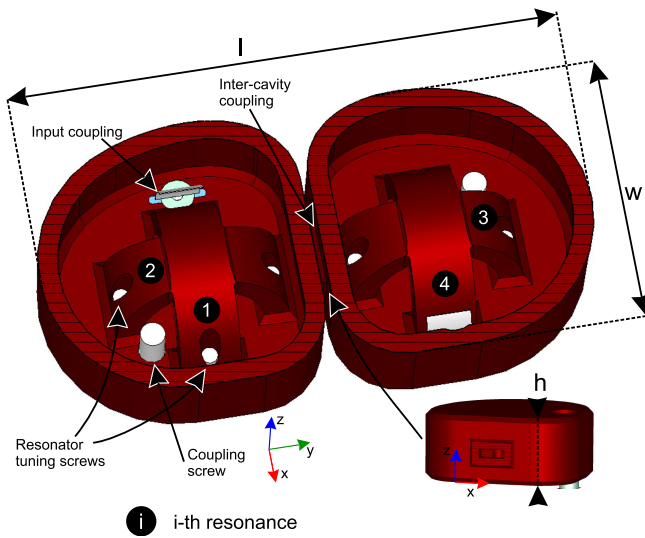


FIGURE 2. Simulation model of the proposed monolithic prototype (cover not shown). Outer dimensions of the housing: $w = 33.88$ mm, $l = 67$ mm, and $h = 14$ mm.

processed material as well as on the choice of temperature and time planned for debinding. Subsequently, the component is sintered at a much higher temperature. At this point, the component has the desired ceramic properties such as mechanical strength and electrical characteristics. Depending on the required material specifications, post-processing steps such as grinding and polishing, can be applied.

III. FILTER DESIGN

The scope of this project is the realization of a monolithic ceramic TM dual-mode filter with the following electrical specifications: The center frequency is $f_0 = 6$ GHz and the minimum required bandwidth is $B_{min} = 150$ MHz ($f_{l,min} = 5.925$ GHz, $f_{u,min} = 6.075$ GHz). The desired return loss is set to $RL = 23$ dB. Two X-shaped dual-mode resonators are used to realize a fourth order bandpass filter. As discussed in [24], X-shaped dual-mode resonators can realize transmission zeros by proper arrangement. However, in order to fulfill the desired specifications, transmission zeros are not necessarily required. The proposed filter structure is shown in Fig. 2, where all resonances are denoted by black circles. Each resonator consists of a bent X-shaped ceramic, which is dimensioned to employ two orthogonal TM_{010} modes. Both resonant modes are coupled by a coupling screw while the cavities are coupled by an iris aperture. In comparison to conventional dielectric filters, not only the resonators consist of ceramic material but the housing as well. The outer dimensions of the housing are given as $w = 33.88$ mm and $l = 67$ mm. The height of the filter is designed to be $h = 14$ mm. The exterior of the housing will be metallized by a silver spray in the last manufacturing step.

The filter can be synthesized according to standard techniques [31], which are accomplished as demonstrated in the

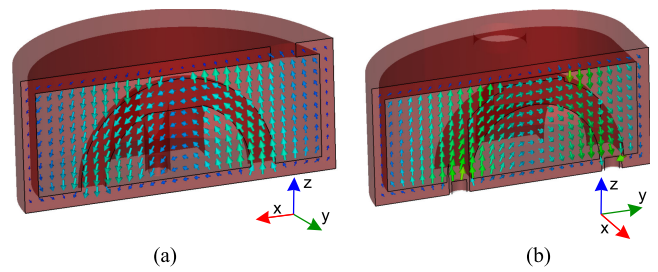


FIGURE 3. Electric field distribution of the eigenmodes: (a) in branch 1 and (b) in branch 2 (compare Figs. 2 and 4).

following. In order to realize a fourth order filter, in a first approximation possibly arising TZs are not considered, as their exact positions are not required to fulfill the desired specifications. The coupling coefficients of a fourth order Chebyshev filter response with a return loss of $RL = 23$ dB without TZs can be calculated by standard techniques [32] and are given as $M_{S1} = M_{4L} = 1.106$, $M_{12} = M_{34} = 0.986$ and $M_{23} = 0.741$. In order to extend the margin in the tuning process, the bandwidth was increased to roughly $B_{sim} = 279$ MHz ($f_{l,sim} = 5.871$ GHz, $f_{u,sim} = 6.15$ GHz, $FBW_{sim} = 4.64\%$). It is worth to mention that the filter response is slightly asymmetric with respect to the desired center frequency. However, the resonator tuning screws are only able to compensate manufacturing tolerances by decreasing the resonance frequency of the resonators, which justifies the slightly increased center frequency.

From the normalized coupling factors the denormalized ones can be calculated to be $k_{12} = k_{34} = 0.0458$ and $k_{23} = 0.0344$ [33]. The external quality factor is $Q_e = 17.63$. The filter design procedure is described in the following sections and is based on an initial estimated ceramic permittivity of 9.4.

A. X-SHAPED DUAL-MODE RESONATOR

Two coupled X-shaped dual-mode resonators are used for the realization of the filter response. In comparison to the approach in [15], [24], the resonators are bent and connected to a common base plate [25]. As already mentioned, the housing is made from ceramic as well. This advantageously avoids the contact problem between a ceramic resonator and the (usually metallic) housing. Furthermore, no alignment problems arise, as the housing and the ceramic resonators are printed in one single piece. Both desired eigenmodes are shown in Fig. 3. As can be seen, the electric field follows the direction of both orthogonal branches and is similar to the classical TM_{010} mode in cylindrical ceramic rods [14]. Due to the orthogonality, the modes are degenerated. The unloaded Q-factor of the resonant modes can be estimated to be $Q_u \approx 7600$. For this estimation, an ideal silver coating as well as a loss tangent of $\tan \delta \approx 4.166 \cdot 10^{-5}$ for the ceramic material is assumed (details to these values are clarified in Section III-E). Furthermore, no tuning screws are considered in these simulations. The required footprint of one dual-mode

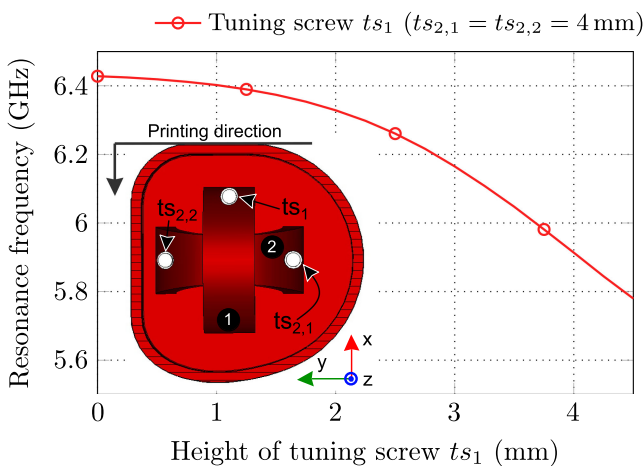


FIGURE 4. Tuning range of the first (vertical) resonance in dependency from tuning screw height ts_1 . The simplified simulation model is shown in the inset. The black arrow indicates the printing direction.

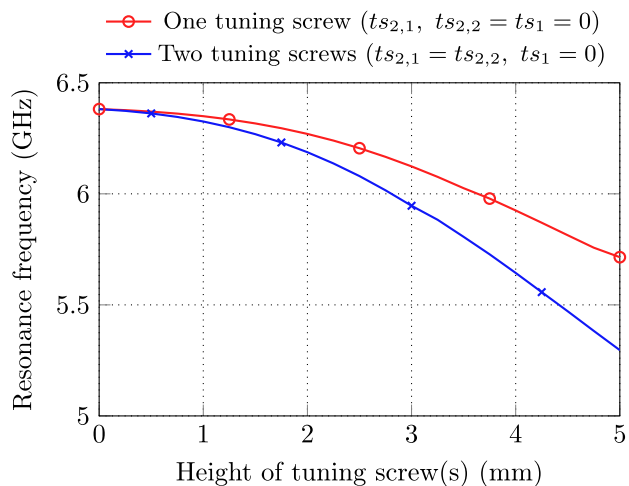


FIGURE 5. Tuning range of the second (horizontal) resonance by using one or both (synchronously tuned) tuning screws ($ts_{2,1}$, $ts_{2,2}$; compare Fig. 4).

cavity is $(w \cdot l)/2 = 1135 \text{ mm}^2$ while the lower and upper spurious modes arise at 4.3 GHz and 7.78 GHz, respectively.

Additionally, it must be mentioned that the housing has an irregular shape due to the adjustment to the 3D printing process, which might lead to a small coupling between both modes.

Tuning screws with a diameter of 2 mm for adjusting the resonance frequencies can be inserted from the base plate into the X-shaped resonator. Two parameter studies are shown in Figs. 4 and 5. The first resonance can only be varied by using one tuning screw. This is due to mechanical reasons, as the input/output coupling must be mounted too close to a possible position of a second tuning screw. Fig. 4 shows the tuning range of the first (vertical) resonance in dependency from the tuning screw height ts_1 . It must be mentioned that the horizontal branch is detuned for this study (e.g. $ts_{2,1} = ts_{2,2} = 4 \text{ mm}$) in order to avoid overlapping resonance frequencies of both

resonances, which would make the evaluation more difficult. The second (horizontal) branch, however, can be tuned by using two tuning screws. This is not necessarily required. Otherwise, a second tuning screw increases the tuning range and offers an additional degree of freedom, e.g. if both tuning screws are asynchronously inserted. The dependency of the resonance frequency of the second resonator from the height of one or even both tuning screws is shown in Fig. 5. As expected, a second tuning screw increases the tuning range.

The shape of the housing is adapted to the printing process as described in Section II. The black arrow in Fig. 4 indicates the printing direction (negative x-direction), starting at the upside of the cavity. The surface is flat to achieve a good adhesion between the housing and the building platform. The lower side of the cavity is rounded in order to reduce the pull-off forces which would occur by printing a flat sidewall. The effect can, however, be reduced by designing the cavity to reveal a kind of dome on the lower side. The form of the X-shaped resonator is adapted to the printing process as well. The horizontal arm shows a necking to the center because the realization of large surfaces parallel to the building platform might lead to cracks or other errors, similar as in the case of the surrounding cavity. Additionally, it must be mentioned, that the shape of the cavity reveals an asymmetry in y-direction as well. The left hand side of the cavity is nearly flat for realizing the inter-cavity coupling as described in Section III-D. An abrupt transition between horizontal and vertical sidewalls might lead to cracks in the sintering process. For this reason, the right-hand side of the cavity wall is completely rounded, because there is no need to provide a flat sidewall. As already shown in Fig. 2, chamfers are added between the resonator and the housing to realize a smooth transition between both. These details are not considered in the simplified simulation models of Figs. 4 and 5.

B. INPUT COUPLING

The form of the input/output coupling is shown in Figs. 2 and 6. It consists of a capacitive plate, which is bent into the direction of the resonator for inherently increasing the coupling strength. The input coupling can be mounted from the bottom of the filter via a slot into the ceramic housing. A further assembly in the filter interior is not possible, as it is printed monolithically without the opportunity for opening.

The external quality factor can be adjusted by the width and height of the plate as well as by the offset to the resonator, denoted as o_i . Fig. 6 shows a parameter study regarding the external quality factor in dependency from the offset of the input coupling. The simplified simulation model is shown in the inset, consisting of only one branch of the former X-shaped resonator. As expected, a larger distance reduces the input coupling strength. To achieve the desired performance, the input coupling should have a distance of roughly 2.2 mm from the first resonator. In this simulation, the width of the plate is assumed to be 5.4 mm and the height is 6.8 mm.

As the filter is printed monolithically, a slot is foreseen in the ceramic housing at the position where the plate will be

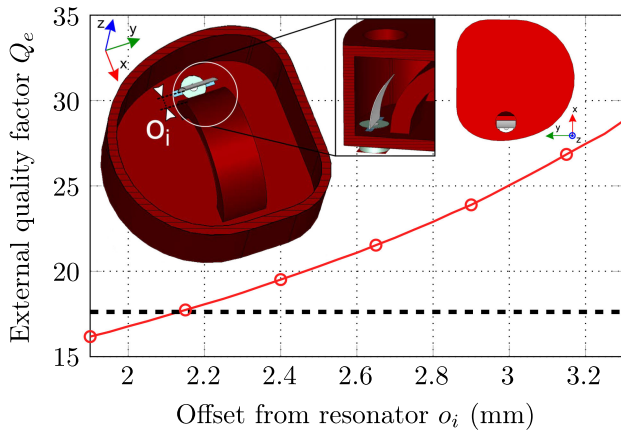


FIGURE 6. External quality factor Q_e in dependency from the offset of the input coupling to the resonator o_i . The simplified simulation model including a close-up of the bent input coupling plate is shown in the inset. The dashed line indicates the desired Q_e value.

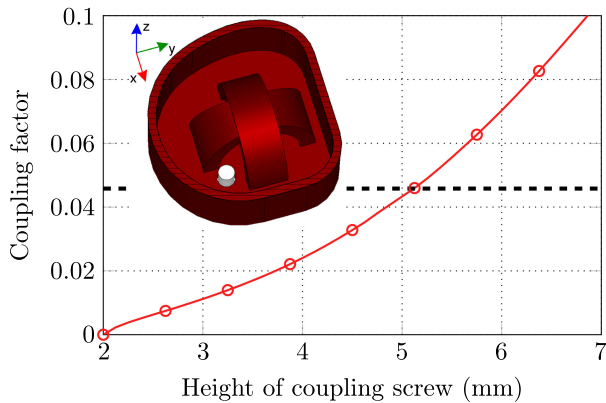


FIGURE 7. Coupling factor k_{12} and k_{34} in dependency from the height of the coupling screw. The inset shows the (simplified) simulation model. The dashed line indicates the desired coupling factor value.

assembled. The whole input coupling consisting of an SMA connector, a piece of wire and the plate itself is therefore assembled individually and then mounted on the ceramic housing. Fine tuning can be accomplished by using a hole in the top cover above the input/output coupling as shown in the right hand side inset of Fig. 6. Through this hole, the plate might be slightly bent into the direction of the resonator (positive x-axis) to allow a tuning of the external quality factor in the assembled filter set-up.

C. INTRA-CAVITY COUPLING

The intra-cavity coupling is required to couple both orthogonal modes of the X-shaped resonator. A coupling screw as shown in the inset of Fig. 7 is used to achieve the desired coupling strength. From Fig. 7 it can be seen, that the deeper the coupling screw is inserted, the higher the coupling factor. It must be mentioned that for this analysis the equation for asynchronously tuned resonators in [31] is used. This is because the resonance frequencies of the individual branches

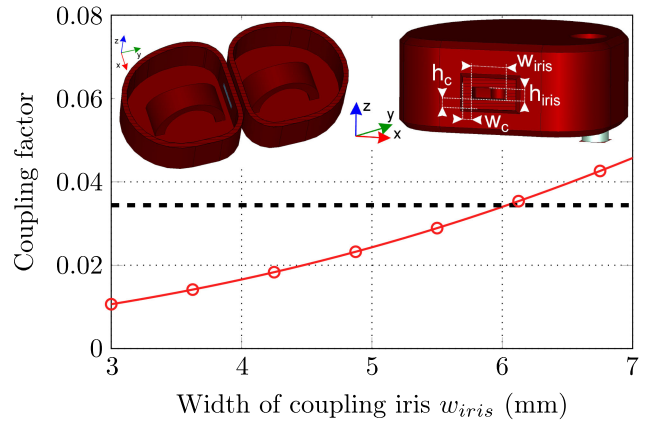


FIGURE 8. Coupling factor k_{23} in dependency from the iris width w_{iris} . The inset shows the (simplified) simulation model as well as the parameters available to control the coupling strength at the inter-cavity coupling.

of the X-shaped resonator are already adapted to the loading effects, which arise in a coupled resonator filter.

D. INTER-CAVITY COUPLING

The inter-cavity coupling is required to couple both resonators for the realization of a fourth order filter. This is accomplished by a simple coupling iris as shown in Figs. 2 and 8 (inset). Different parameters are available to adapt the inter-cavity coupling strength. One obvious parameter is given by the width of the aperture w_{iris} . A parameter study which reveals the coupling factor in dependency from this parameter is shown in Fig. 8. Obviously, a larger iris width leads to a larger coupling factor. In order to achieve the required coupling strength, the width of the iris should be chosen to approximately 6 mm. The simplified model for this investigation is shown in the inset of Fig. 8, where only the required branches of the X-shaped resonator are simulated. Another option to influence the coupling factor is given by the material thickness of the aperture walls w_c and h_c , which contribute to the interaction of the fields as well.

On the one hand, these parameters should not be chosen too small due to mechanical instabilities. Therefore, the realized filter model is chamfered at the transition between the cavity housing and the blend aperture. On the other hand, the ceramic is not allowed to be too thick to be in accordance with the design rules.

E. SIMULATION RESULTS AND MANUFACTURING

The complete filter structure is shown in Fig. 2. To avoid mechanical stress during sintering as well as 90° transitions, all edges of the simulated prototype are either chamfered or reveal radii. This additionally includes edges between the bottom/cover and the side walls, between the bottom and the resonator branches as well as the inter-cavity coupling. Furthermore, radii are added at the cross-point of the X-shaped resonator. The edges on the outside of the cavity are chamfered as well.

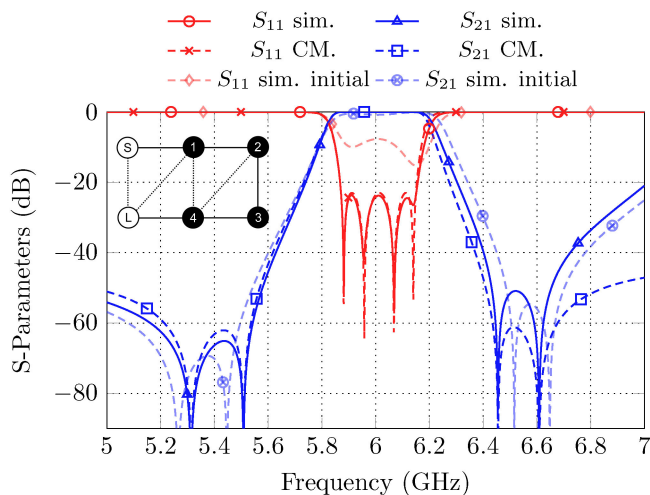


FIGURE 9. Simulation results of the structure from Fig. 2 in comparison to the coupling matrix representation as well as the initial simulation after the filter design process. The inset shows the coupling scheme derived from the simulated S-Parameters with the following coefficients: $M_{11} = 0.011$, $M_{22} = 0.027$, $M_{33} = -0.108$, $M_{44} = 0.010$, $M_{51} = 1.098$, $M_{12} = 0.966$, $M_{23} = 0.769$, $M_{34} = 0.962$, $M_{4L} = 1.098$, $M_{24} = 0.09$, $M_{14} = -0.093$, $M_{1L} = -0.007$, $M_{5L} = 0.004$.

The simulated S-Parameter results in comparison to the coupling matrix representation as well as the initial S-Parameters after the filter design process are shown in Fig. 9. For the initial simulation all parameters as an outcome of the design process described above are used. However, it must be mentioned that the resonator tuning screws are already set into the final position as all resonators are designed for a slightly higher frequency than required. This circumstance is necessary in order to be able to compensate tolerances “in both directions”. Furthermore, all radii and chamfers are neglected in the filter design process. However, as a one-to-one relationship between the coupling matrix entries (at least for the mainline couplings) and the available tuning elements can be identified, the optimization is a straight forward task using coupling matrix extraction and tuning techniques. As can additionally be seen in Fig. 9, in total four slightly asymmetric TZs at normalized frequencies $f_{TZ,LP} = \{-j5.31, -j3.75, j3.09, j4.1\}$ arise. The inner TZ pair might be associated with a cross-coupling between resonator 1 and 4. Based on the large distance between these resonators, this coupling is very weak. The outer TZ pair might be interpreted as a parasitic source to load coupling, which is caused by the integral effect of higher/lower order modes [34]. Spurious modes in the simulated filter are located below and above the passband at frequencies 4.1 GHz and 7.3 GHz, respectively. The TZs might be slightly moved in their frequency by varying the position of the inter-cavity coupling.

The coupling scheme associated with the filter response is shown in the inset of Fig. 9 with all coupling factors given in the caption. The diagonal cross couplings are introduced to take into account the asymmetry of the TZs - i.e. the classical canonical form as introduced in [32] is applied. This model

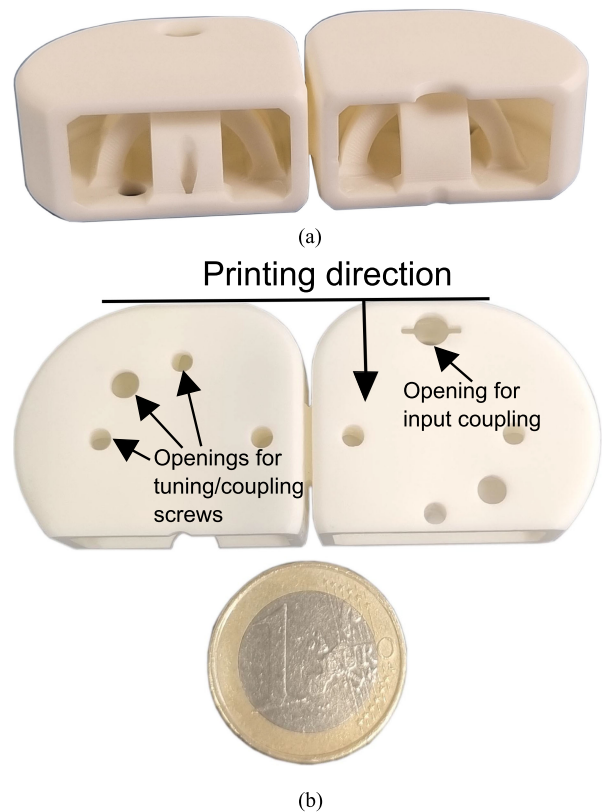


FIGURE 10. Partially printed filter for validation purposes: (a) inside view and (b) illustration of the printing direction as well as size comparison with a 1 euro coin.

uses the narrow-band approximation with frequency independent coupling values. Alternatively, one might also consider frequency dependent coupling factors (but this is beyond the scope of this paper). The coupling matrix representation in Fig. 9 describes the filter behaviour sufficiently well below the passband while there are discrepancies for higher frequencies. These deviations are mainly caused by the already mentioned higher order modes, which are not included in the coupling matrix description. As all TZs are relatively far away from the passband, the design approach discussed in Section III with the all-pole coupling factors as design goal gives a meaningful first approximation. However, the final S-Parameter response in Fig. 9 is obtained by using coupling matrix extraction and tuning techniques as well as a final full wave optimization. This is especially required, as all chamfers and radii were neglected in the initial dimensioning - since they limit the handling of the simulation model with respect to parameter variations - but are required for the filter printing process.

A prototype of a manufactured filter is shown in Fig. 10. For validation purposes, the fabrication of the filter was not completed but stopped after printing the vertical branches of the X-shaped resonators. Fig. 10(a) gives an internal view of the prototype whereas (b) indicates the printing direction and provides a size comparison with a 1 euro coin. The manufactured filter is realized in alumina material with permittivity

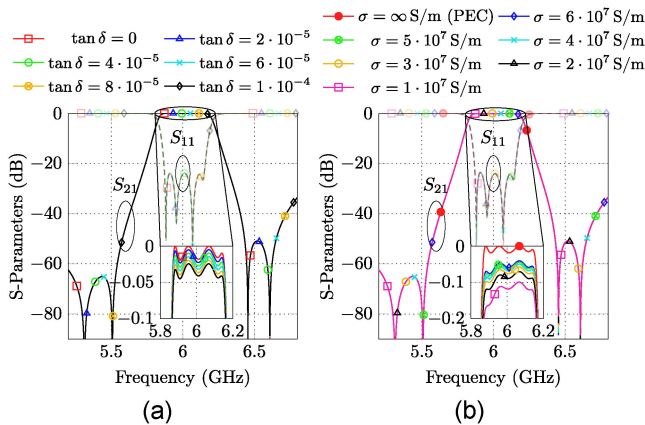


FIGURE 11. Parameter studies: (a) ideal simulation from Fig. 9 including losses in the ceramic material and (b) ideal simulation from Fig. 9 including finite conductivity of the housing.

$\epsilon_r \approx 9.32$ and unloaded Q-factor $Q_u \approx 24.000$ (loss tangent $\tan \delta \approx 4.2 \cdot 10^{-5}$) estimated at 5.27 GHz.

For material characterization a resonator which is excited in the $TE_{01\delta}$ -mode is used. A cylindrical test geometry is placed in the center of the cavity, which is made from copper and weakly excited by using wires. The loss tangent is estimated in two different ways: On the one hand, the measurement methods described in [35, Sec. 2.4.7.3] are employed. By using the proposed equations, the unloaded Q-factor can be calculated from measured S_{11} and S_{21} data in different ways. However, all other loss mechanisms (e.g. losses in the SMA connectors, the losses of the holder material as well as the finite conductivity of the cavity itself) are measured as well and lower the Q-factor. Therefore, this method defines a lower bound of the Q-factor to be estimated. On the other hand, the resonator is simulated in a full wave simulator including the losses of the cavity as well as the feeding lines. Subsequently, the S-Parameters of the measurement are compared to those of the simulation while the material parameters are altered until a matching of both is achieved. This additionally allows the estimation of the real part of the permittivity.

Furthermore, Fig. 11(a) shows a parameter study with respect to dielectric losses of the ideal simulation in Fig. 9. The $\tan \delta$ is varied between $\tan \delta_{min} = 0$ (lossless) and $\tan \delta_{max} = 1 \cdot 10^{-4}$. Obviously, even for a dielectric loss tangent, which is 2.4 times higher than the measured one, the insertion loss in the passband is smaller than 0.05 dB. A similar study is done in Fig. 11(b), where the conductivity of the metallization is varied between $\sigma_{max} = \infty$ S/m (PEC) and $\sigma_{min} = 10$ MS/m. A low conductivity seems to have a more serious effect on the insertion loss, as even a metallization with conductivity similar to brass leads to insertion losses higher than 0.1 dB.

Please note, that the prototype in Fig. 10 is not metallized at this point. The final demonstrator reveals a silver layer applied with an airbrush aerosol [36]. As the surface of the ceramic is very smooth, it is required to roughen it by sand blasting in order to provide a meaningful adhesion between the ceramic and the metal coating. The applied coating is specified to

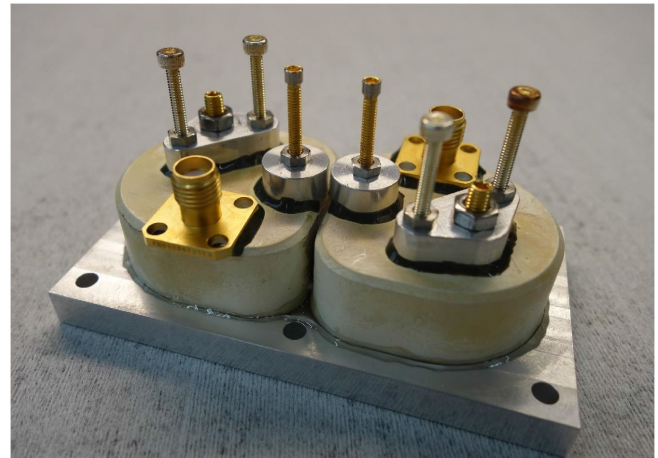


FIGURE 12. Measurement set-up with all tuning screws and SMA connectors mounted on the silver coated surface.

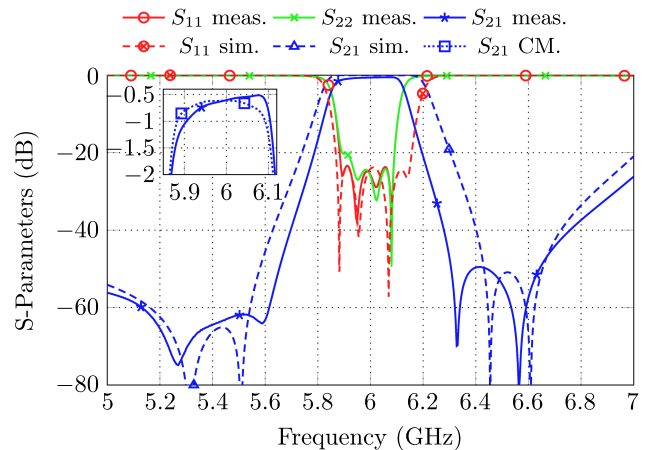


FIGURE 13. Measurement results of the filter in Fig. 12 in comparison to the simulation.

reveal a thickness of $4 \mu\text{m}$. On the one hand, the skin depth at a center frequency of 6 GHz and by assuming an ideal silver conductivity is $0.83 \mu\text{m}$. The coating therefore reveals a thickness of roughly five times the skin depth. On the other hand, after applying between three and four micrometers of the proposed aerosol, the surface resistance tends to that of pure silver [36].

IV. MEASUREMENT RESULTS AND DISCUSSION

A. MEASUREMENT SET-UP AND RESULTS

Fig. 12 shows the metallized filter with all connectors and tuning screws mounted. All tuning screws are guided by specialized holders. These holders as well as the SMA connectors are glued with Eccobond CE8500 to the silver coated surface of the filter.

The measurement results in comparison to the simulation are shown in Fig. 13. The input reflection coefficient is matched to at least 23 dB within the passband edges between $f_{l,meas} = 5.887$ GHz and $f_{u,meas} = 6.089$ GHz ($B_{meas} = 202$ MHz, $f_{0,meas} = 5.987$ GHz, $FBW_{meas} = 3.37\%$). The

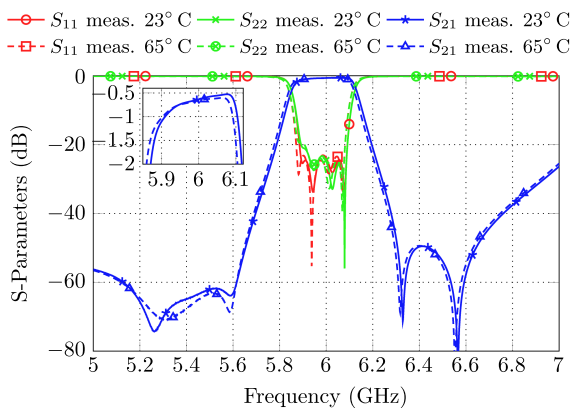


FIGURE 14. Temperature stability measurement.

output reflection coefficient is slightly worse and matched to at least 20 dB. It is worth to mention that the filter meets the minimum required bandwidth specifications of 150 MHz. However, a significant bandwidth reduction compared to the simulated filter arises. This must be attributed to the inter-cavity coupling (coupling M_{23}), which is realized by a simple aperture and designed to be not-tunable. By utilizing coupling matrix extraction techniques, a normalized coupling factor of $M_{23} \approx 0.57$, which is about 23% lower compared to the desired one, can be extracted. All other couplings as well as the input/output coupling might be tuned in the assembled filter and are therefore not primarily responsible for the bandwidth reduction. However, in the manufactured prototype the coupling strengths of all tunable couplings are adapted to achieve an equi-ripple performance. Potential reasons for the decreased coupling factor are deviations in the ceramic 3D printing process as well as a potentially unequal shrinkage in the sintering process due to an irregular mass distribution of ceramic material. Furthermore, it must be mentioned that an asymmetric tuning of the tuning screws in the horizontal branches can lead to a coupling factor reduction as well.

The inset in Fig. 13 gives a close view on the transmission coefficient S_{21} around the filter center frequency. Obviously, the transmission in the passband is rather slanted and the TZs on the lower passband side are weakly pronounced. One obvious reason might be a crack in the inter-cavity coupling, which arises during mounting the filter on a base plate to ease the measurement and tuning process. This crack was glued with a conductive glue (Eccobond CE8500). The unloaded Q-factor is estimated to be $Q_u \approx 840$ based on characteristic filter polynomials. The corresponding transmission coefficient S_{21} is plotted in the inset of Fig. 13 as well and denoted as CM (coupling matrix).

B. TEMPERATURE STABILITY

The results of the temperature stability investigation of the filter are shown in Fig. 14. The initial measurement takes place at room temperature (23°C) while the second measurement was executed at 65°C . The 23 dB band edges at room temperature are located at $f_{l,cold} = 5.89\text{ GHz}$ and $f_{u,cold} =$

6.088 GHz while they are shifted to $f_{l,warm} = 5.874\text{ GHz}$ and $f_{u,warm} = 6.078\text{ GHz}$ at 65°C . The exact center frequency of both measurements might be calculated to be $f_{0,cold} = 5.9882\text{ GHz}$ and $f_{0,warm} = 5.975\text{ GHz}$, leading to a center frequency downward shift of 13.1 MHz or 0.22% (52.087 ppm).

V. CONCLUSION

This paper describes the design and realization of a fourth order TM mode dielectric resonator filter. The filter is manufactured using a ceramic additive manufacturing approach called LCM. The AM technique is described and compared to the basically similar stereolithography approach. Subsequently, the filter design process is outlined, including the dimensioning of the input coupling as well as the intra- and inter-resonator coupling. A prototype is manufactured in alumina and subsequently spray coated with a silver surface. The measurement results show good agreement to the simulation apart from a reduction of the bandwidth. A coupling matrix extraction reveals, that the coupling between both dual-mode cavities is too small, reducing the achievable bandwidth to 202 MHz. The unloaded Q-factor is estimated to be $Q_u \approx 840$ while a temperature drift of 0.22% between room temperature and 65°C can be measured.

ACKNOWLEDGMENT

The authors acknowledge financial support by DFG within the funding programme Open Access Publikationskosten.

REFERENCES

- [1] R. D. Richtmyer, "Dielectric resonators," *J. Appl. Phys.*, vol. 10, no. 6, pp. 391–398, Jun. 1939.
- [2] S. J. Fiedziuszko and S. Holmes, "Dielectric resonators raise your high-Q," *IEEE Microw. Mag.*, vol. 2, no. 3, pp. 50–60, Sep. 2001.
- [3] R. R. Mansour, "Filter technologies for wireless base stations," *IEEE Microw. Mag.*, vol. 5, no. 1, pp. 68–74, Mar. 2004.
- [4] J.-F. Liang and W. D. Blair, "High-Q TE₀₁ mode DR filters for PCS wireless base stations," *IEEE Trans. Microw. Theory Techn.*, vol. 46, no. 12, pp. 2493–2500, Dec. 1998.
- [5] D. D. Fernando, I. C. Hunter, and V. Postoyalko, "A novel dual-mode TE_{01s} dielectric resonator," in *MTT/ED/AP/LEO Societies Joint Chapter United Kingdom and Republic of Ireland Section. 1999 High Frequency Postgraduate Student Colloquium (Cat. No.99TH8409)*, IEEE, Sep. 1999, pp. 48–53. [Online]. Available: <https://ieeexplore.ieee.org/document/809279>
- [6] K. Wakino, T. Nishikawa, and Y. Ishikawa, "Miniaturization technologies of dielectric resonator filters for mobile communications," *IEEE Trans. Microw. Theory Techn.*, vol. 42, no. 7, pp. 1295–1300, Jul. 1994.
- [7] C. Guo, X. Shang, M. J. Lancaster, and J. Xu, "A 3-D printed lightweight X-band waveguide filter based on spherical resonators," *IEEE Microw. Wireless Compon. Lett.*, vol. 25, no. 7, pp. 442–444, Jul. 2015.
- [8] C. Guo, X. Shang, J. Li, F. Zhang, M. J. Lancaster, and J. Xu, "A lightweight 3-D printed X-band bandpass filter based on spherical dual-mode resonators," *IEEE Microw. Wireless Compon. Lett.*, vol. 26, no. 8, pp. 568–570, Aug. 2016.
- [9] N. Delhote, D. Baillargeat, S. Verdeyme, C. Delage, and C. Chaput, "Narrow Ka bandpass filters made of high permittivity ceramic by layer-by-layer polymer stereolithography," in *Proc. IEEE Europ. Microw. Conf.*, 2006, pp. 510–513.
- [10] N. Delhote, D. Baillargeat, S. Verdeyme, C. Delage, and C. Chaput, "Ceramic layer-by-layer stereolithography for the manufacturing of 3-D millimeter-wave filters," *IEEE Trans. Microw. Theory Techn.*, vol. 55, no. 3, pp. 548–554, Mar. 2007.

- [11] N. Delhote, D. Baillargeat, S. Verdeyme, C. Delage, and C. Chapat, "Innovative shielded high Q dielectric resonator made of alumina by layer-by-layer stereolithography," *IEEE Microw. Wireless Compon. Lett.*, vol. 17, no. 6, pp. 433–435, Jun. 2007.
- [12] D. B. N. Delhote, M. Chatras, and S. Verdeyme, "Ku band filter based on low loss alumina octagonal dielectric resonators made by 3D ceramic stereolithography," in *Proc. IEEE Europ. Microw. Conf.*, 2009, pp. 1397–1400.
- [13] M. Höft and T. Magath, "Compact base-station filters using TM-mode dielectric resonators," in *Proc. German Microw. Conf.*, 2006, pp. 1–4.
- [14] M. Höft, "Bandpass filter using TM-mode dielectric rod resonators with novel input coupling," in *IEEE MTT-S Int. Microw. Symp. Dig.*, 2009, pp. 1601–1604.
- [15] P. Rezaee and M. Höft, "A new class of compact dual-mode dielectric resonator filters," in *Proc. IEEE MTT-S Int. Microw. Symp.*, 2016, pp. 1–3.
- [16] D. Miek, P. Boe, F. Kamrath, and M. Höft, "Dielectric TM dual-mode filters with Y-shape," in *Proc. IEEE MTT-S Int. Microw. Filter Workshop*, 2021, pp. 69–72.
- [17] P. Boe, D. Miek, F. Kamrath, and M. Höft, "Triple-mode bandpass filter based on TM dielectric rod resonators," in *Proc. IEEE MTT-S Int. Microw. Symp.*, 2021, pp. 499–502.
- [18] T. Nishikawa, Y. Ishikawa, J. Hattori, K. Wakino, and Y. Kobayashi, "4 GHz band band-pass filter using an orthogonal array coupling TM₁₁₀ dual mode dielectric resonator," in *Proc. 19th Europ. Microw. Conf.*, 1989, pp. 866–891.
- [19] J. Hattori, H. Kubo, S. Abe, T. Nishiyama, and Y. Ishikawa, "Compact transmitting dielectric resonator filter using capacitive loaded dual mode method for PCS microcellular base station," in *IEEE MTT-S Int. Microw. Symp. Dig.*, 1996, pp. 1631–1634.
- [20] C. Carceller, F. Gentili, W. Bösch, D. Reichartzeder, and M. Schwen-tenwein, "Ceramic additive manufacturing as an alternative for the development of miniaturized microwave filters," in *Proc. IEEE MTT-S Int. Microw. Workshop Ser. Adv. Mater. Processes RF THz Appl.*, 2017, pp. 1–3.
- [21] C. Carceller, F. Gentili, D. Reichartzeder, W. Bösch, and M. Schwen-tenwein, "Development of monoblock TM dielectric resonator filters with additive manufacturing," *IET Microw. Antennas Propag.*, vol. 11, no. 14, pp. 1992–1996, Oct. 2017.
- [22] S. W. Sattler, F. Gentili, R. Teschl, C. Carceller, and W. Bösch, "Emerging technologies and concepts for 5G applications - A making additive manufactured ceramic microwave filters ready for 5G," in *Proc. IEEE Int. Symp. VLSI Techn. Syst. Appl.*, 2018, pp. 1–6.
- [23] Q. Liu *et al.*, "Additive manufacturing of monolithic microwave dielectric ceramic filters via digital light processing," *Electronics*, vol. 8, no. 10, Sep. 2019, Art. no. 1067.
- [24] D. Miek, S. Salzer, and M. Höft, "Realization of cross-coupled X- and Y-shaped dual-mode dielectric resonator filters," in *Proc. IEEE Asia-Pacific Microw. Conf.*, 2018, pp. 506–508.
- [25] K. K. Karhu, "Dual-mode resonator," U.S. Patent 6650208B2, Nov., 2003. [Online]. Available: <https://patents.google.com/patent/US6650208B2/en>
- [26] A. Khalil *et al.*, "Compact low loss alumina band-pass filter in Ku band using layer-by-layer stereolithography technology," in *IEEE MTT-S Int. Microw. Symp. Dig.*, 2009, pp. 1469–1472.
- [27] L. Carpentier, N. Delhote, S. Verdeyme, L. Estagerie, H. Leblond, and D. Pacaud, "Compact Ku band filter based on BMT dielectric resonators made in a single part using 3D ceramic stereolithography process," in *IEEE/MTT-S Int. Microw. Symp. Dig.*, 2012, pp. 1–3.
- [28] Y. Marchives, N. Delhote, S. Verdeyme, and P. M. Iglesias, "Wide-band dielectric filter at C-band manufactured by stereolithography," in *Proc. IEEE 44th Eur. Microw. Conf.*, 2014, pp. 187–190.
- [29] A. Perigaud, O. Tantot, N. Delhote, S. Verdeyme, S. Bila, and D. Baillargeat, "Bandpass filter based on skeleton-like monobloc dielectric pucks made by additive manufacturing," in *Proc. IEEE 48th Eur. Microw. Conf.*, 2018, pp. 296–299.
- [30] Lithoz. [Online]. Available: <https://www.lithoz.com/en>
- [31] J.-S. Hong, *Microstrip Filters for RF/Microwave Applications*, 2nd ed. K. Chang, Ed. Hoboken, NJ, USA: Wiley, 2011.
- [32] R. J. Cameron, "Advanced coupling matrix synthesis techniques for microwave filters," *IEEE Trans. Microw. Theory Techn.*, vol. 51, no. 1, pp. 1–10, Jan. 2003.
- [33] R. J. Cameron, C. M. Kudsia, and R. R. Mansour, *Microwave Filters for Communication Systems: Fundamentals, Design, and Applications*, 2nd ed. Hoboken, NJ, USA: Wiley, 2018.
- [34] P. Boe, D. Miek, F. Kamrath, and M. Höft, "Hybrid inline TE/TM mode dielectric resonator filters with wide spurious free range and controllable transmission zeros," in *Proc. IEEE 50th Eur. Microw. Conf.*, 2021, pp. 555–558.
- [35] L. F. Chen, C. K. Ong, C. P. Neo, V. V. Varadan, and V. K. Varadan, *Microwave Electronics Measurement and Materials Characterisation*. Hoboken, NJ, USA: Wiley, 2004.
- [36] Jet metal. [Online]. Available: <https://www.jetmetal-tech.com/the-firm?lang=en>



DANIEL MIEK (Student Member, IEEE) was born in Minden, Germany, on January 10, 1992. He received the B.Sc. and M.Sc. degrees in electrical engineering and information technology from the University of Kiel, Kiel, Germany, in 2015 and 2017, respectively, where he is currently working toward the Dr.-Ing. degree with the Department of Electrical and Information Engineering. He is a member of the Chair of Microwave Engineering with the Department of Electrical and Information Engineering, University of Kiel. His research inter-

ests include the design, realization, and optimization of waveguide and dielectric filters.



MICHAEL HÖFT (Senior Member, IEEE) was born in Lübeck, Germany, in 1972. He received the Dipl.-Ing. degree in electrical engineering and Dr.-Ing. degree from the Hamburg University of Technology, Hamburg, Germany, in 1997 and 2002, respectively. From 2002 to 2013, he was with Communications Laboratory, European Technology Center, Panasonic Industrial Devices Europe GmbH, Lüneburg, Germany. He was a Research Engineer and then team leader, where he was engaged in the research and development of

microwave circuitry and components, particularly filters for cellular radio communications. From 2010 to 2013, he was a group leader for the research and development of sensor and network devices. Since October 2013, he has been a Full Professor with the Faculty of Engineering, Kiel University, Kiel, Germany, where he is also the Head of the Microwave Group with the Institute of Electrical and Information Engineering. His research interests include active and passive microwave components, (sub-) millimeter-wave quasi-optical techniques and circuitry, microwave and field measurement techniques, microwave filters, microwave sensors, and magnetic field sensors.

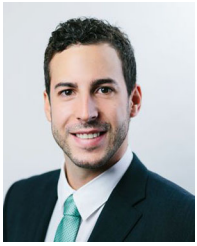
Dr. Höft is a member of the European Microwave Association, the Association of German Engineers (VDI), and German Institute of Electrical Engineers (VDE).



JOSE ANTONIO LORENTE was born in Murcia, Spain, in 1984. He received the M.Sc. degree in telecommunications engineering and the Ph.D. degree from the Technical University of Cartagena, Cartagena, Spain, in 2008 and 2013, respectively. In 2007, he joined the Telecommunication and Electromagnetic Group, Technical University of Cartagena, as a Research Assistant. From 2008 to 2011, he was with European Space Agency (ESA/ESTEC) under Networking Partnering Initiative (NPI) Program, where he developed new

techniques for loss reduction in waveguide filters by geometry optimization. Since 2012, he has been with Passive Products Section with Tesat Spacecom, Backnang, Germany, where he is responsible for the development of mainly commercial high power filters and output networks and also the design and development of new products, including 3D optimized geometries.

ANDRE BERGER, photograph and biography not available at the time of publication.



DOMINIK BROUCZEK was born in Salzburg, Austria, in 1989. He received the B.Sc. and M.Sc. degrees in technical chemistry from the Vienna University of Technology, Vienna, Austria, in 2014 and 2018, respectively. In 2017, he joined Lithoz, Vienna, Austria, where he is currently a Materials Engineer with R&D Department for the development of ceramic materials and photo-curable suspensions for additive manufacturing, and contributing to international and national research projects in the field of materials and application development.



MARTIN SCHWENTENWEIN received the Ph.D. degree in chemical engineering and photopolymer chemistry from Vienna University of Technology, Vienna, Austria, in 2012. In 2012, he joined Lithoz, Vienna, Austria, where he is currently the Head of Materials Development and R&D Coordinator.

ANA BRANDAO, photograph and biography not available at the time of publication.



PETRONILO MARTÍN-IGLESIAS (Member, IEEE) was born in Caceres, Spain, on April 23, 1980. He received the Telecommunication Engineering degree from the Polytechnic University of Madrid, Madrid, Spain, in 2002, and the master's degree from The University of Leeds, Leeds, U.K., in 2012. He has been with industry for more than ten years as a Microwave Engineer involved with active (high power amplifiers for radar applications) and passive (filters, multiplexers, and couplers) RF hardware

design, including two years as a Radar System Engineer with Indra Sistemas, ISDEFE S.A., and Thales Alenia Space Spain. Since 2012, he has been involved with research and development and project support activities related with RF passive hardware developments with the European Space Agency. Since January 2021, he has been a part of the Earth Observation Future Microwave Instruments Section with ESA-ESTEC. His research interests include filter synthesis theory, electromagnetic design and high power prediction, and advanced manufacturing techniques for RF passive hardware.



VITTORIO TORNIELLI DI CRESTVOLANT (Member, IEEE) was born in Reggio Emilia, Italy, in 1986. He received the Laurea Triennale degree in telecommunications engineering from the University of Parma, Parma, Italy, the Laurea Specialistica degree from the Politecnico di Milano, Milan, Italy, in 2010, and the Ph.D. degree from the University of Birmingham, Birmingham, U.K., in 2015, under the supervision of Prof. M. Lancaster, in a Network/Partnering Initiative (NPI) with the European Space Agency, Noordwijk, The

Netherlands, and Airbus Defence and Space, Stevenage, U.K. In 2016, he joined the Feeds and Filters Group, Airbus Defence and Space, as an RF Design Engineer. In 2019, he joined the RF Equipment and Technology Section, ESA/ESTEC, with responsibilities in the domain of passive microwave equipment, such as filters, multiplexers, couplers, and isolators. His research interests include the synthesis and design of microwave filters and multiport distribution networks with inherent filter transfer functions, based on all-resonator circuits and novel techniques for the design of additive manufacturing filters and multiplexers.